Journal of Zhejiang University-SCIENCE A (Applied Physics & Engineering)
ISSN 1673-565X (Print); ISSN 1862-1775 (Online)
www.jzus.zju.edu.cn; www.springerlink.com
E-mail: jzus@zju.edu.cn

Forming quality, mechanical properties, and anti-inflammatory activity of additive manufactured Zn–Nd alloy*

Ci-jun SHUAI[1,2,3], Ming-li YANG[1], Fang DENG[1], You-wen YANG[†‡1,4], Shu-ping PENG[†‡5,6],
Fang-wei QI[1], Chong-xian HE[1], Li-da SHEN[4], Hui-xin LIANG[4]

[1] *Institute of Bioadditive Manufacturing, Jiangxi University of Science and Technology, Nanchang 330013, China*
[2] *State Key Laboratory of High Performance Complex Manufacturing, Central South University, Changsha 410083, China*
[3] *Shenzhen Institute of Information Technology, Shenzhen 518172, China*
[4] *Jiangsu Key Laboratory of Precision and Micro-Manufacturing Technology,*
Nanjing University of Aeronautics and Astronautics, Nanjing 210016, China
[5] *School of Basic Medical Science, Central South University, Changsha 410083, China*
[6] *School of Energy and Machinery Engineering, Jiangxi University of Science and Technology, Nanchang 330013, China*
[†] E-mail: yangyouwen@csu.edu.cn; shuping@csu.edu.cn

Received Apr. 27, 2020; Revision accepted June 3, 2020; Crosschecked Oct. 16, 2020

Abstract: Zinc (Zn) has recently been recognized as a promising bone repair material due to its inherent biodegradability and favorable biocompatibility. In this work, rare earth neodymium (Nd) was introduced into a Zn-based alloy fabricated using a laser powder bed fusion (LPBF) process. Results showed that addition of Nd significantly improved the melt fluidity and reduced the evaporation of Zn, thereby achieving parts with a high densification rate of 98.71%. Significantly, the Nd alloying treatment effectively refined the grain size from 25.3 to 6.2 µm. $NdZn_5$ eutectics precipitated and contributed to a second-phase strengthening effect. As a result, the tensile strength increased to (119.3±5.1) MPa and the Vickers hardness to (76.2±4.1). Moreover, the Zn–Nd alloy exhibited good anti-inflammatory activity, as the Nd ions released during degradation had a strong affinity with cell membrane phospholipids and consequently inhibited the release of inflammatory cytokines. It also presented favorable cytocompatibility, showing great potential as a bone repair material.

Key words: Zn–Nd alloy; Laser powder bed fusion (LPBF); Anti-inflammatory activity; Mechanical properties
https://doi.org/10.1631/jzus.A2000186 **CLC number:** TG146.13; TG665; R318.08

1 Introduction

In the last ten years, zinc (Zn) has become known as a promising material for bone defect repair, since it has inherent biodegradability and favorable biocompatibility (Zhu SM et al., 2019). Zn has a moderate corrosion potential of −0.7 V, which enables it to degrade by means of electrochemical corrosion in physiological environments (Wei et al., 2019). Its degradation products, namely Zn ions, play a crucial role in enzymatic catalysis, cell metabolism, and immune function (Baltaci et al., 2018). Recently, Zn scaffolds with a porous structure have been proposed for bone tissue engineering (Wen et al., 2018a, 2018b). Unfortunately, Zn exhibits insufficient mechanical strength to satisfy the requirements of a bone implant, especially for load-bearing functions. Also,

---

[‡] Corresponding author

[*] Project supported by the National Natural Science Foundation of China (Nos. 51935014, 82072084, and 81871498), the Jiangxi Provincial Natural Science Foundation of China (Nos. 20192ACB20005 and 2020ACB214004), the Jiangxi Provincial Key R&D Program (No. 20201BBE51012), the Guangdong Provincial Higher Vocational Colleges & Schools Pearl River Scholar Funded Scheme (2018), the China Postdoctoral Science Foundation (No. 2020M682114), the Open Research Fund of Jiangsu Key Laboratory of Precision and Micro-Manufacturing Technology, and the Project of Hunan Provincial Science and Technology Plan (No. 2017RS3008), China

ORCID: You-wen YANG, https://orcid.org/0000-0003-1557-0252

inflammation usually occurs during bone repair, which will undoubtedly reduce the service quality of Zn-based implants.

Alloying is a feasible strategy to improve the mechanical strength of metal materials (Pariona and Micene, 2019). Rare earth elements, Cu (Niu et al., 2016; Tang et al., 2017; Hou et al., 2018; Yue et al., 2019; Shuai et al., 2020e), Mg (Yang et al., 2018), etc. have been proposed as promising alloying elements. Especially, rare earth elements, known for their surface activity and large atomic radius, can easily interrupt grain growth and form stable compounds as alloying elements, thus contributing to a combination of grain refinement and second-phase strengthening (Wang et al., 2019). For example, Xu et al. (2017) reported that neodymium (Nd) caused grain refinement of the Mg alloy, thereby improving its ultimate tensile strength, yield strength, and elongation. Li W et al. (2019) confirmed that yttrium led to grain refinement in the Ti alloy. Plotkowski et al. (2017) reported that addition of cerium to the Al alloy formed intermetallic $Al_{11}Ce_3$ and enhanced the hardness. Nd ions have a strong affinity with cell membrane phospholipids and can stabilize on the surface of cell membranes, thereby inhibiting the release of pro-inflammatory cytokines (Li RB et al., 2014; Yao et al., 2016). They can also induce the synthesis of anti-inflammatory factors due to the antagonist effect of calcium (Shi et al., 2017; Zhu DY et al., 2019). Moreover, Nd has been reported to have favorable biocompatibility (Shuai et al., 2017).

Based on the above considerations, in this study Nd was alloyed with Zn to improve mechanical strength and simultaneously endow anti-inflammatory activity. The Zn–Nd part was fabricated using laser powder bed fusion (LPBF). This method is a representative laser additive manufacturing technique which uses a laser beam as an energy source to melt powder, and then builds parts in a layer-by-layer fashion (Liu et al., 2018; Zhu et al., 2018; Paz et al., 2019; Yang YW et al., 2020, 2021). In general, this alloying treatment can greatly affect the forming quality (such as the densification rate and surface quality), since a metallurgical reaction might occur in response to the radiation of the laser. Therefore, the forming quality, microstructural features, and mechanical properties of the alloy were systematically studied, and their relationships elaborated. The anti-inflammatory property, corrosion behavior, and cytotoxicity were also evaluated in relation to the potential application of this alloy to bone defect repair.

2 Materials and methods

2.1 Material and sample fabrication

Zn powder (20–50 μm) and Nd powder (5–15 μm) were used in this work. Zn and Nd powders with a content of 1%, 3%, and 5% in weight were mixed using a planetary mill with a ball-to-powder ratio of 10:1, for 2 h. The Nd powder with its small particle size exerted no obvious negative effect on the powder fluidity, since the content of Nd powder was very small. A laser additive manufacturing system was adopted to carry out the experiments. The system was composed of a fiber laser, a scanning galvanometer, a building chamber, and an atmosphere circulation system to produce an argon atmosphere with oxygen content below 0.1 g/m^3. A scanning strategy was adopted that first scanned in the *X*-direction and then turned 90° in the *Y*-direction for each layer, as shown schematically in Fig. 1a. This strategy was believed to be able to overcome any blockage of the laser beam by evaporated particles. The process parameters were optimized after several pre-experiments, and set as follows: laser power 50 W, scanning rate 300 mm/s, hatch space 0.06 mm, laser spot-diameter 0.07 mm, and thickness 0.07 mm. The obtained Zn–xNd (x=0, 1%, 3%, 5% in weight) parts with a size of 6 mm×6 mm×6 mm are shown in Fig. 1b.

2.2 Microstructural characterization

The surfaces of the laser additive manufactured Zn–xNd parts were observed using a scanning electron microscope (SEM, EVO 18, Zeiss, Germany). The samples were then polished using SiC grinding papers, and etched using nitric acid solution (4% in volume). The microstructure was investigated using an optical microscope (OM, DM2700, Leica, Germany) and SEM combined with an energy dispersive spectroscope (EDS, X–Max 20, Oxford Instruments, the UK). The phase composition was determined using an X-ray diffractometer (XRD, D8 Advance, Karlsruhe, Germany) with Cu Kα radiation.

2.3 Mechanical tests

The samples used in this work were fabricated according to the standard of metallic stretching splines (ISO, 2019) (Fig. 1c). The tensile tests were carried out using a universal tensile testing machine (Metes Industrial Systems Co. Ltd., China) at a crosshead speed of 1 mm/min. The fracture surfaces were observed by SEM. Hardness tests were carried out using a microhardness tester (Beijing TIME High Technology Co. Ltd., China) with a 0.98-N load and a holding time of 15 s.

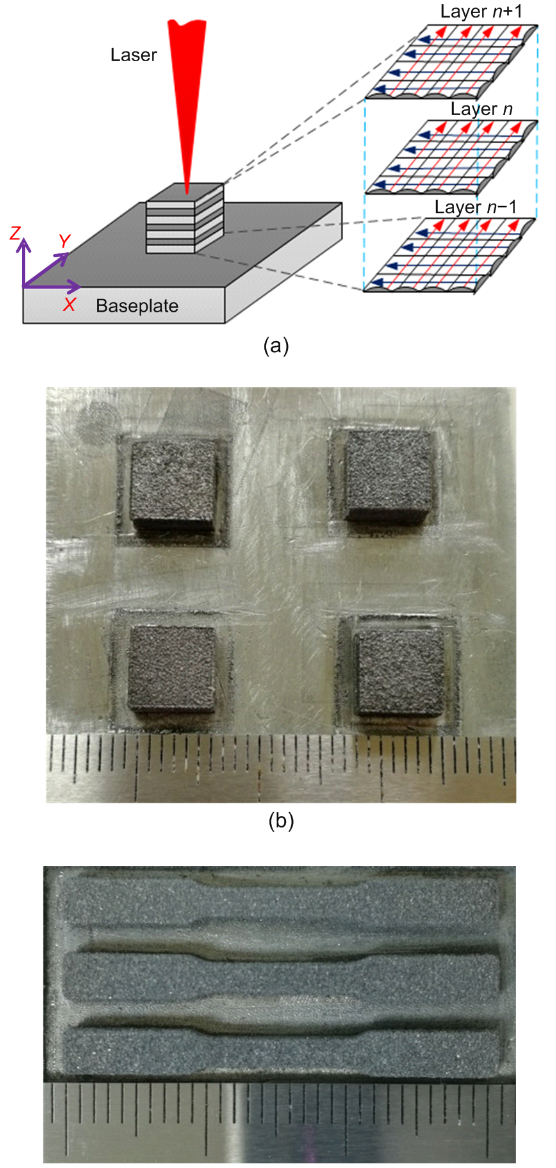

(a)

(b)

(c)

Fig. 1 Laser scanning strategy (a), as-built Zn–*x*Nd (*x*=0, 1%, 3%, 5% in weight) parts (b), and tensile samples (c)

2.4 Electrochemical and immersion experiments

Electrochemical tests were conducted using an electrochemical working system (CHI604D, CH Instruments Inc., China) in simulated body fluid (SBF, 37 °C, pH 7.4). A three-electrode cell consisting of a platinum counter-electrode, a saturated calomel electrode, and a working electrode was used. The parts, sealed in paraffin wax, were first immersed in SBF for 2000 s to obtain the open circuit potential. Subsequently, Tafel curves were recorded at a scanning rate of 0.05 mV/s. The Nyquist plots and electrochemical impedance tests (100 kHz to 0.01 Hz) were also performed.

SBF immersion tests were implemented to investigate the corrosion behavior of as-built parts according to ASTM G31-72 (ASTM, 2004). The ratio of each sample's surface area to solution volume was 0.1 cm^2/mL. Specimens soaked in SBF for 7, 14 or 28 d were washed with distilled water. The corrosion surface was then observed by SEM.

2.5 Evaluation of anti-inflammatory activity

The anti-inflammatory activities of Zn–3Nd and Zn were tested using the murine macrophage cell line RAW264.7 (Chinese Academy of Sciences). Before testing, the samples were cleaned twice using phosphate buffered saline (PBS) and then dried. Cells were incubated in Dulbecco's modified Eagle medium (DMEM, HyClone, the USA) supplemented with 10% fetal bovine serum (FBS, HyClone, the USA). After several passages, the cells were seeded on Zn–3Nd and Zn samples and placed on 24-well plates for 1, 4 or 7 d in a humidified environment. Subsequently, the cells were washed twice using PBS and then stained using calcein-AM reagents. The stained cells were observed using a fluorescence microscope (BX60, Olympus Co., Japan).

A cell counting Kit-8 (CCK-8) assay was also performed. After the cells were cultured for 1, 4 or 7 d, CCK-8 solution (Sigma-Aldrich, the USA) was added to each well and cultured for 4 h. The absorbance was obtained at 450 nm using a paradigm detection platform (Beckman, CA, the USA). At 4 and 7 d, total RNA was extracted using Trizol reagent (Life Technologies, the USA) and transcribed using PrimeScript RT reagent kit (Takara, Japan). The cDNA was amplified and detected using a Roche LightCycler480 real-time polymerase chain reaction (PCR) system

(Takara, Japan). The relative expression levels of genes were standardized with the internal control (GAPDH) by adopting the $2^{-\Delta\Delta Ct}$ method (Jin et al., 2019).

2.6 Cytotoxicity assay

In vitro cell tests were carried out using MG-63 cells in accordance with ISO 10993-5:2009 (ISO, 2009). Before the tests, Zn and Zn–3Nd specimens were soaked in DMEM containing 10% FBS and 10% penicillin-streptomycin for 72 h, to prepare extracts at a ratio of 1.25 cm^2/mL. Cells were then incubated in the extracts for 1, 4 or 7 d. Subsequently, the cells were stained using calcein-AM and ethidium homodimer-1 reagent, and visualized by microscopy. MG-63 cells incubated in DMEM were used as a control. After 1, 4 or 7 d, cells were cultured with CCK-8 solution for 2 h. The cell viability was also determined using a paradigm detection platform.

2.7 Statistical analysis

All experiments were triplicated, with results expressed in format “mean±deviation”. Student’s

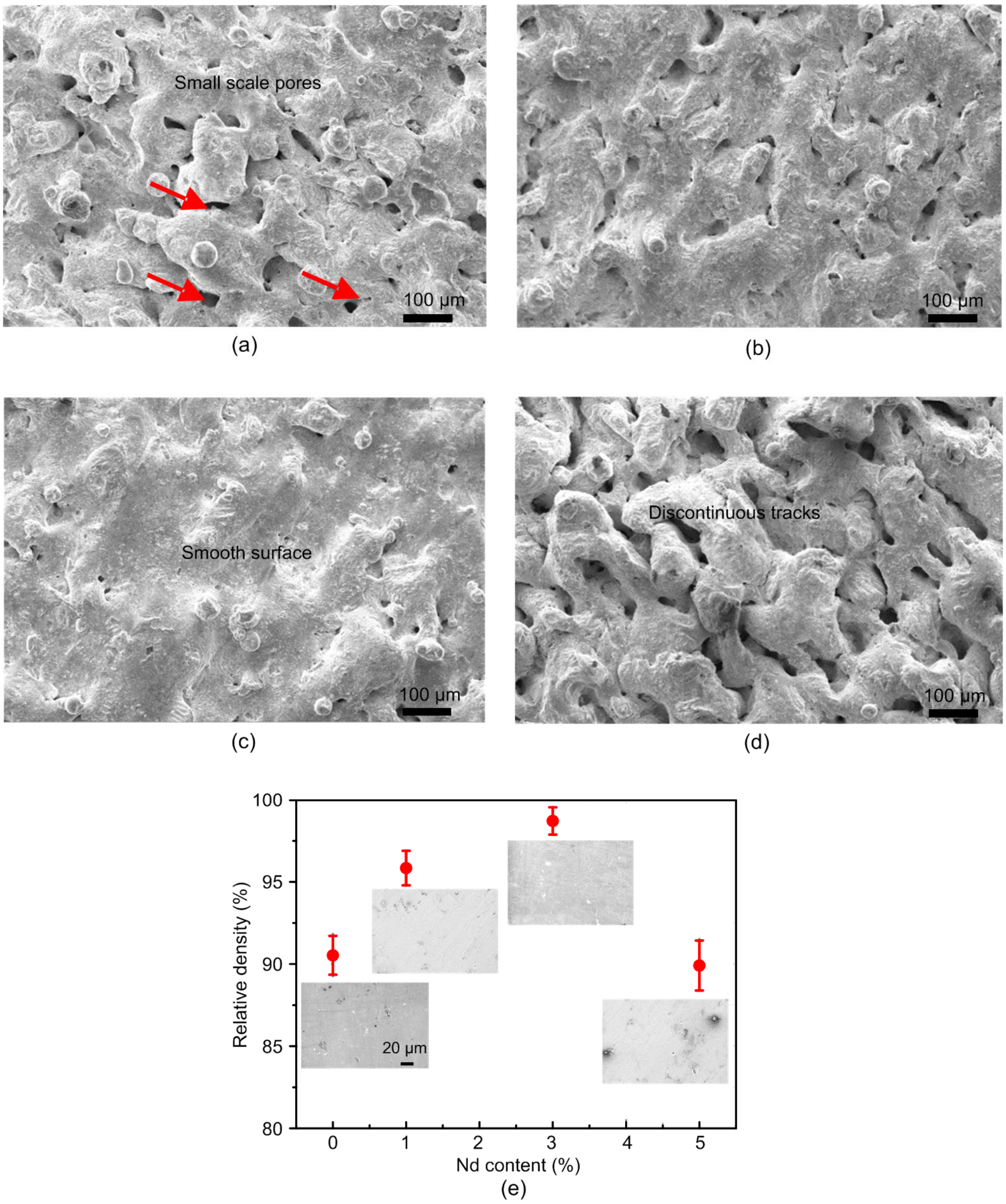

(a) (b) (c) (d) (e)

Fig. 2 Surface morphologies of laser additive manufactured Zn–*x*Nd parts: (a) Zn; (b) Zn–1Nd; (c) Zn–3Nd; (d) Zn–5Nd; (e) densification rates of as-built Zn–*x*Nd parts (the inserts show typical cross-sections of Zn–*x*Nd parts)

t-test was carried out to investigate the significance. A *p* value of less than 0.05 was considered significant.

3 Results

3.1 Formation quality and microstructure evolution

The surface morphologies of laser additive manufactured Zn–*x*Nd parts were observed by SEM (Fig. 2) (p.879). A rough surface with numerous open-pores appeared on the Zn part (Fig. 2a). The pores appearing on the surface of the Zn–1Nd part were considerably reduced (Fig. 2b). As for Zn–3Nd, a relatively smooth surface with a continuous scanning trace was achieved, indicating its improved forming quality. With Nd further increased, the scanning trace turned discontinuous with a large number of large-scale pores appearing (Fig. 2d). The corresponding densification rates of laser additive manufactured Zn–*x*Nd parts were calculated, with results shown in Fig. 2e. The densification rates of all

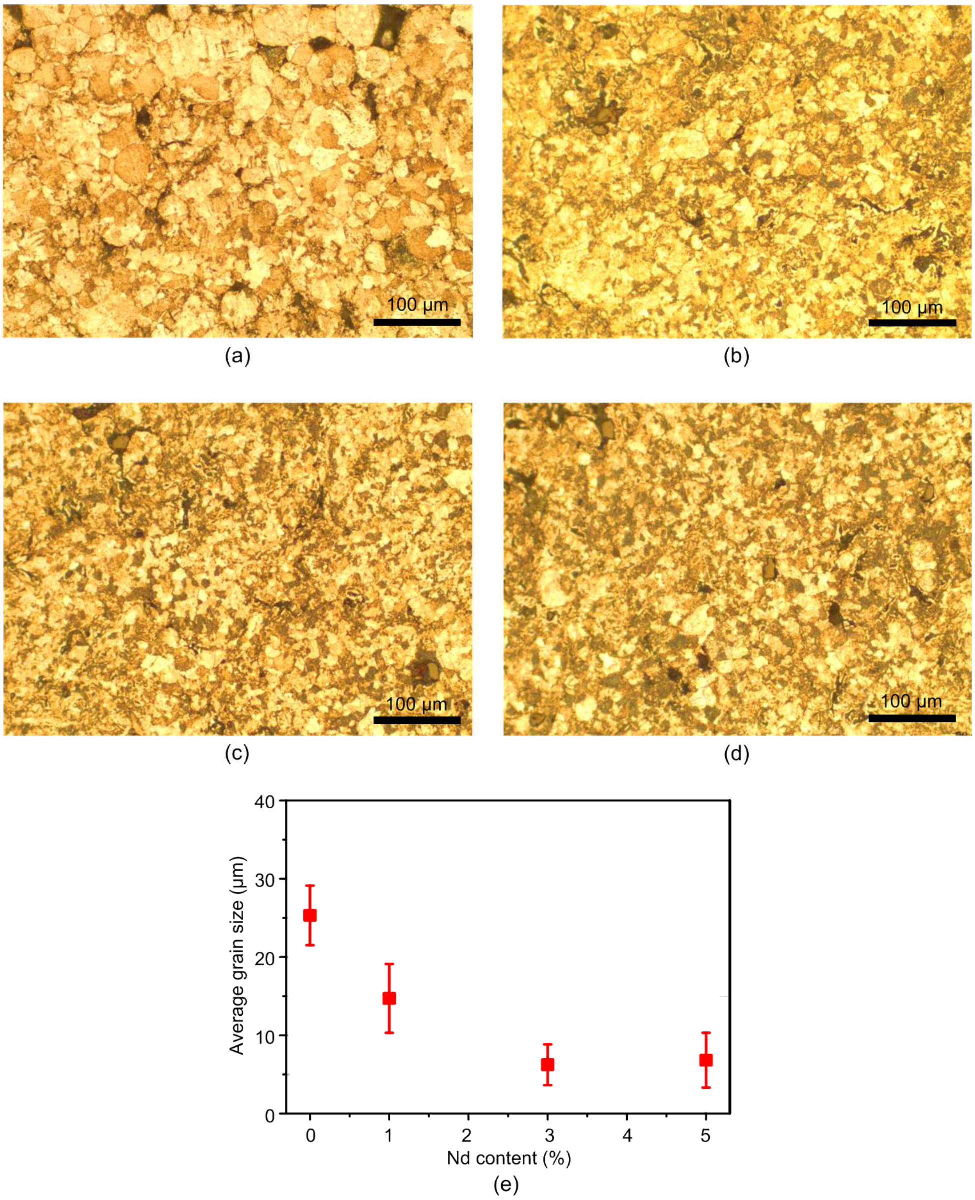

Fig. 3 OM images of laser additive manufactured Zn–*x*Nd parts: (a) Zn; (b) Zn–1Nd; (c) Zn–3Nd; (d) Zn–5Nd; (e) average grain size

samples were analyzed by measuring the porosity with Image J software. The Zn–3Nd part achieved an extremely high densification rate of 98.71%, while the Zn part reached only 90.53%. Mass Zn evaporation usually occurs during LPBF, causing unstable laser energy deposition, which would significantly influence the densification rate (Montani et al., 2017). The microstructure of laser additive manufactured Zn–*x*Nd parts was investigated by OM (Fig. 3) (p.880). Uniform and fine equiaxed grains were observed for all parts. It is well known that laser additive manufacturing involves rapid solidification, which favors the formation of a fine and homogeneous microstructure. Notably, Nd alloying treatment further refined the crystal structure, with an average grain size of (6.2±2.6) μm for Zn–3Nd.

The microstructure of the Zn–*x*Nd parts was further investigated by SEM in a backscatter model (Fig. 4). A duplex microstructure was clearly observed in the matrix of Zn–*x*Nd parts. The precipitated second phase, consisting mainly of Zn and Nd, became massive as Nd increased, and showed a discontinuous distribution. EDS analysis also revealed that a small amount of Nd had dissolved in the Zn matrix. The precipitated second phase segregated and aggregated in the matrix of Zn–5Nd.

The phase composition was investigated by XRD, with collected spectra depicted in Fig. 4f. The laser additive manufactured Zn–*x*Nd parts were composed mainly of Zn and $NdZn_5$ phase. Furthermore, a close-up view of the patterns from 42° to 45° revealed that the principal diffraction peak of the Zn phase slightly shifted negatively with increasing Nd. According to Bragg's law (Brooks et al., 2018),

$$2d\cdot\sin\theta = N\cdot\lambda, \tag{1}$$

where λ is the wavelength, N is the reflection series, θ is the angle between incident light and crystal plane, and d is the lattice parameter. The shifted diffraction peaks were likely caused by the increased lattice parameters. Nd has a larger atomic radius (182 pm) than Zn (135 pm). After the alloying treatment, partial Nd atoms dissolved in the Zn matrix, thereby increasing the interplanar spacing.

3.2 Mechanical properties

The mechanical properties of as-built Zn–*x*Nd parts were investigated by tensile tests, with the tensile properties shown in Table 1. Zn had a relatively low ultimate tensile strength of only (66.5±6.5) MPa, and an elastic modulus of (58.4±8.6) GPa. After alloying with Nd, the ultimate tensile strength and elastic modulus of Zn–3Nd were significantly enhanced to (119.3±5.1) MPa and (79.4±5.3) GPa, respectively. The elongation gradually decreased from (10.2±2.3)% to (6.7±1.6)%. Nevertheless, further addition of Nd slightly decreased the tensile strength to (107.3±6.2) MPa. The Vickers hardness was also tested, and gradually increased from (56.5±6.7) to (82.2±5.4).

Typical fracture surfaces of Zn–*x*Nd parts after tensile tests were observed by SEM (Fig. 5) (p.883). Many cleavage steps and cleavage planes surrounded by tearing ridges were clearly observed on the Zn part (Fig. 5a). This indicates a typical cleavage fracture mode, with the fracture surface separated along a certain crystal surface. As the Nd was increased, cleavage planes increased and became small (Figs. 5b and 5c). In particular, river patterns along smooth cleavage planes appeared on Zn–3Nd. Small and shallow dimples were also observed, which indicated a mixed transgranular and intergranular fracture mode. Some cracks were propagated through the grains. As for Zn–5Nd, large-scale cleavage planes with few dimples were observed, indicating an increased brittleness.

3.3 Corrosion behavior

Electrochemical tests were performed to investigate corrosion behavior, with the results shown in

Table 1 Tensile properties and hardness of laser additive manufactured Zn–*x*Nd parts

Sample	Ultimate tensile strength (MPa)	Elongation (%)	Elastic modulus (GPa)	Vickers hardness
Zn	66.5±6.5	10.2±2.3	58.4±8.6	56.5±6.7
Zn–1Nd	96.3±4.9	8.7±1.9	67.4±7.7	67.2±5.1
Zn–3Nd	119.3±5.1	6.7±1.6	79.4±5.3	76.2±4.1
Zn–5Nd	107.3±6.2	4.3±1.8	85.4±6.1	82.2±5.4

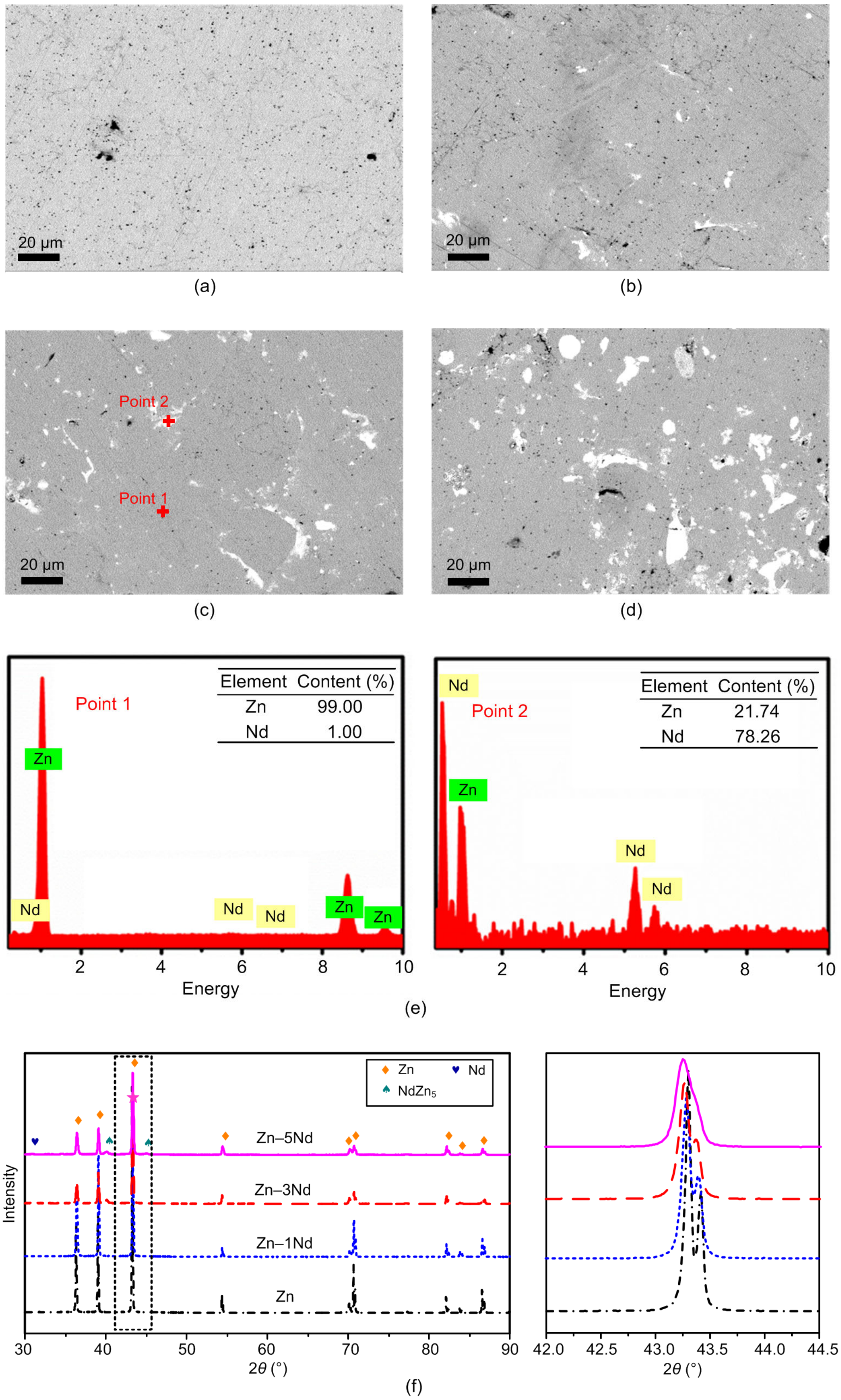

Fig. 4 Cross-section microstructure of laser additive manufactured Zn–*x*Nd parts: (a) Zn; (b) Zn–1Nd; (c) Zn–3Nd; (d) Zn–5Nd; (e) EDS analysis of points 1 and 2 as marked in Fig. 4c; (f) XRD spectra of as-built Zn–*x*Nd parts

Fig. 6. All the potentiodynamic polarization curves had similar shapes (Fig. 6a), indicating the same electrochemical reaction process. The fitted corrosion potential (E_{corr}) and corrosion current density (i_{corr}) obtained from the Tafel area extrapolations are shown in Fig. 6b. The E_{corr} ranged from −1.12 to −0.96 V. As Nd increased, i_{corr} decreased from (11.84±1.12) $\mu\mathrm{A/cm}^2$ (Zn) to (6.99±0.75) $\mu\mathrm{A/cm}^2$ (Zn–5Nd). The electrochemical impedance spectra (EIS) are shown in Figs. 6c and 6d. The Nyquist plots appear to show a single capacitive loop (Fig. 6c). The diameter of the capacitive loop of Zn–3Nd was slightly higher than that of the other samples, reflecting its relatively high charge transfer resistance. Zn–3Nd also had a higher phase angle and impedance than the other parts (Fig. 6d), indicating enhanced corrosion resistance to some extent.

Immersion tests were performed to further study the corrosion behavior, with the results shown in Fig. 7. A general view showed that all samples preserved an integrated surface without large-scale corrosion pits or crevices, even after immersion for 28 d, suggesting they had suffered only slight and uniform corrosion. A closer SEM observation revealed tiny amounts of flocculent corrosion products. EDS analysis confirmed the corrosion products consisted of Zn, O, C, Na, P, Ca, and Nd. Basing on previous literature, the degradation products of Zn and Nd are Zn hydroxy carbonate ($\mathrm{Zn_4CO_3(OH)_6 \cdot H_2O}$) and Nd oxide, respectively (Yao et al., 2014). In general, the corrosion surface observations indicated that Nd alloying enhanced corrosion resistance to a small extent, since fewer corrosion products were found on Zn–3Nd part than on the Zn part.

3.4 Anti-inflammatory properties

Zn–3Nd with optimal mechanical properties and a moderate degradation rate was used to determine the anti-inflammatory properties, with the Zn part serving as a control. Macrophage cells, one of the first cell types to make contact with bone implants, were used to induce immunogenic reactions. Cells of a murine macrophage cell line cultured on Zn–3Nd and Zn parts for 1 d or 4 d are shown in Fig. 8a (p.885). In

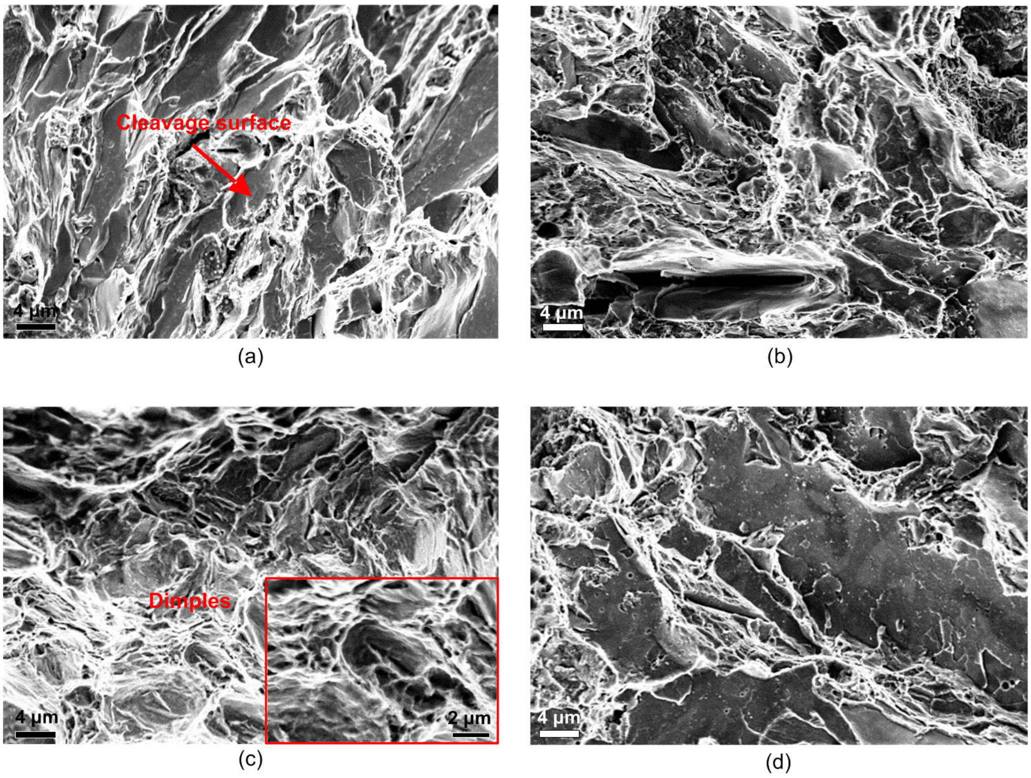

(a) (b) (c) (d)

Fig. 5 Fracture surfaces of laser additive manufactured Zn–*x*Nd parts
(a) Zn; (b) Zn–1Nd; (c) Zn–3Nd; (d) Zn–5Nd

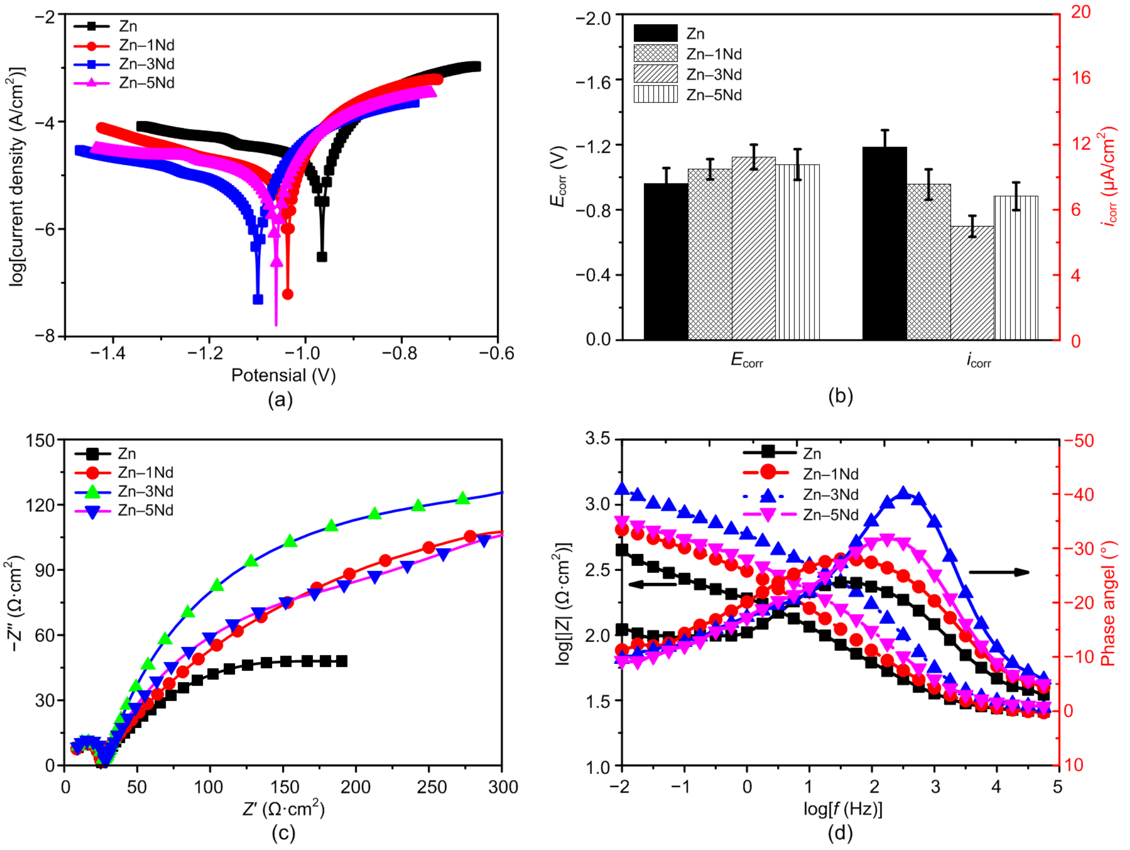

Fig. 6 Electrochemical testing results of laser additive manufactured Zn–*x*Nd parts in SBF: (a) potentiodynamic polarization curves; (b) electrochemical parameters obtained from the Tafel area extrapolations; (c) Nyquist plots; (d) Bode plots

Z′ is the real part of the composite impedance of sample surface; *Z*″ is the imaginary part of the impedance; *f* is the frequency of sinusoidal signal; |*Z*| is the mode of the impedance

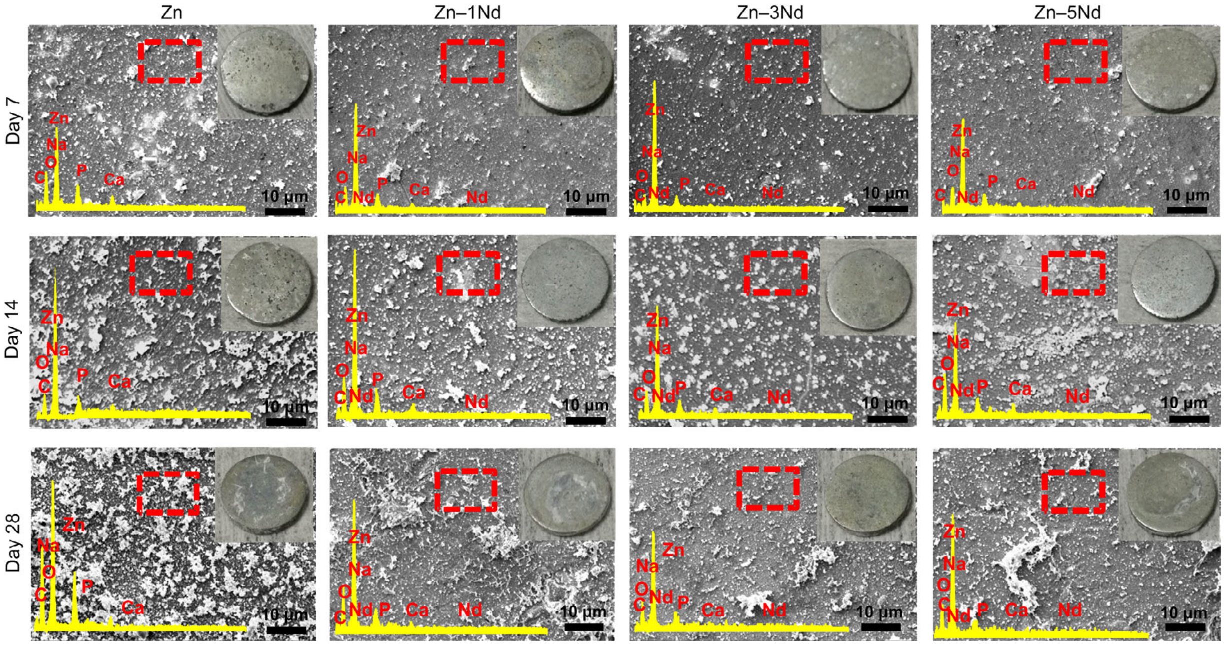

Fig. 7 SEM images showing corrosion surfaces of Zn–*x*Nd parts after immersion in SBF for 7, 14 or 28 d, each with a general view inserted

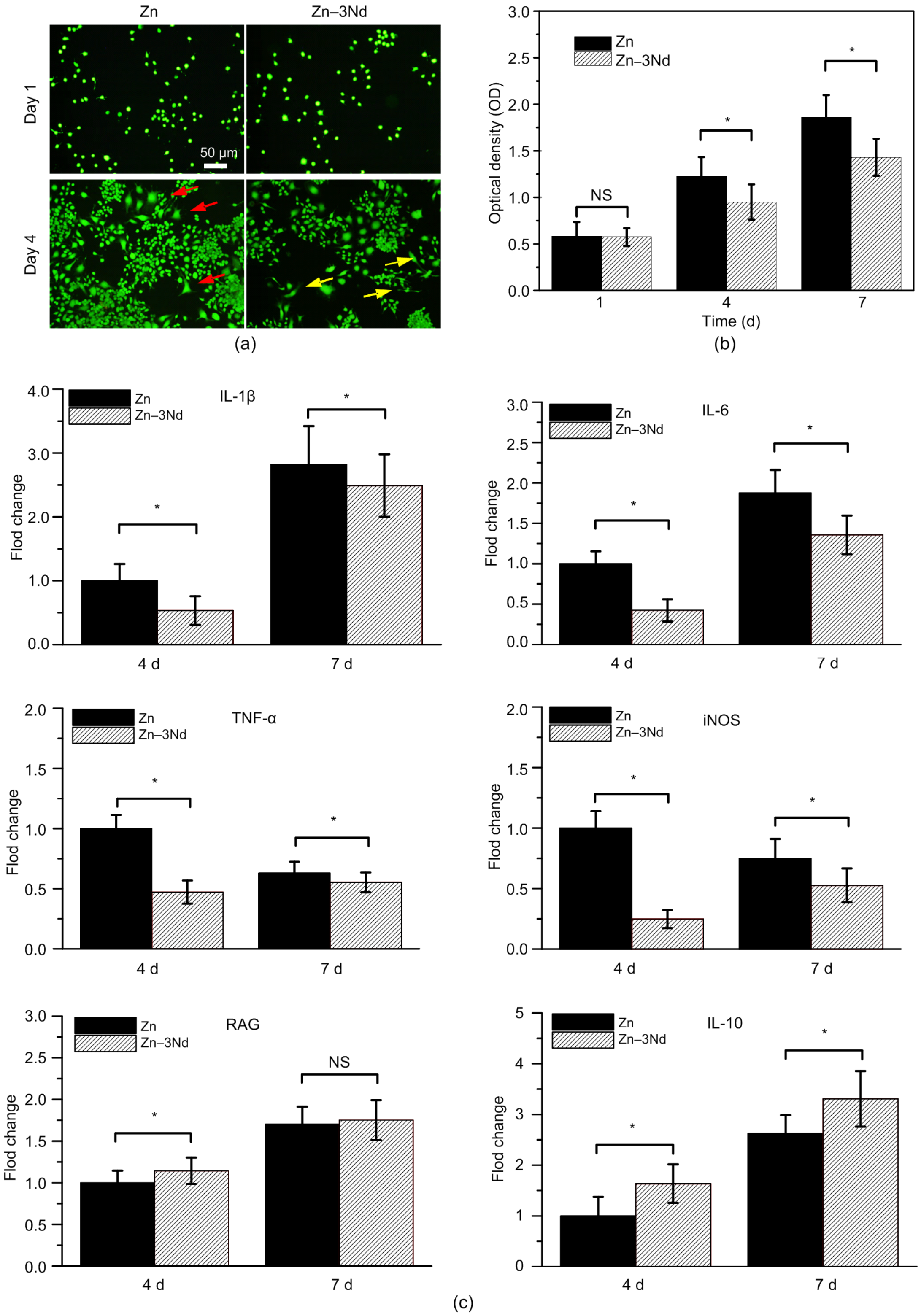

Fig. 8 Inflammatory testing results of macrophages cultured on as-built Zn–3Nd and Zn parts for 1, 4, or 7 d
(a) Morphologies of the macrophages; (b) Proliferation of macrophages; (c) Inflammatory gene expression of IL-1β, IL-6, TNF-α, iNOS (inducible nitric oxide synthase), RAG (recombination-activating gene), and IL-10 in macrophages after 4 or 7 d. Yellow arrow: spindle-shaped cell; red arrow: cell with more pseudopodia; *: $p<0.05$; NS: no significant difference; TNF: tumor necrosis factor. References to color refer to the online version of this figure

general, the macrophages increased as the culture time extended. Significantly, there were fewer cells present on the Zn–3Nd part than on the Zn part after 4-d culture. Morphologically, the macrophages on Zn–3Nd had a round spindle shape at day 4, whereas those on the Zn part were extended with more pseudopodia. These results showed that the macrophages on Zn–3Nd were less active than those on the Zn part.

The proliferation of macrophages was assessed by CCK-8 assay, with the results shown in Fig. 8b. The macrophages increased as incubation time increased, which was consistent with the fluorescence observations. The Zn–3Nd exerted no influence on the macrophages at day 1, but considerably limited the proliferation of macrophages at days 4 and 7. The expression of inflammatory genes was determined quantitatively using real-time PCR (Fig. 8c). Compared with the expression of pro-inflammatory genes on Zn, the expression of IL-6 and iNOS on the Zn–3Nd part was significantly reduced at days 4 and 7 ($p<0.05$). The expression of IL-1β and TNF-α on Zn–3Nd part was also reduced at days 4 and 7 ($p<0.05$). In addition, the Zn–3Nd part improved the expression of the anti-inflammatory genes IL-10 and RAG at days 4 and 7, but the improvement was not significant for RAG at day 7. These results show that compared with Zn, the Zn–3Nd part reduced the pro-inflammatory gene expression and enhanced the anti-inflammatory gene expression.

3.5 Cytotoxicity

Bone implants need not only good mechanical properties and a suitable degradation rate, but also good biocompatibility (Shuai et al., 2019b, 2020a; Cao et al., 2020). In this study, the cytotoxicity of Zn–3Nd was tested using MG-63 cells. Cells cultured for 1, 4 or 7 d are shown in Fig. 9a. In general, the cells increased considerably with the extension of the culture period. The cells at day 4 presented a fusiform shape, indicating normal cell development. In addition, the cell viability was studied quantitatively via a CCK-8 assay, with the results shown in Fig. 9b. No significant differences were observed between the two groups. A cell viability of over 75% is considered acceptable (Li P et al., 2019). Herein, the viability of cells cultured in the Zn–3Nd extract was 78.9% at day 4 and 85.6% at day 7, compared with 81.3% at day 4 and 88.7% at day 7 in the Zn extract. These results indicate that both Zn and Zn–3Nd had favorable cytocompatibility.

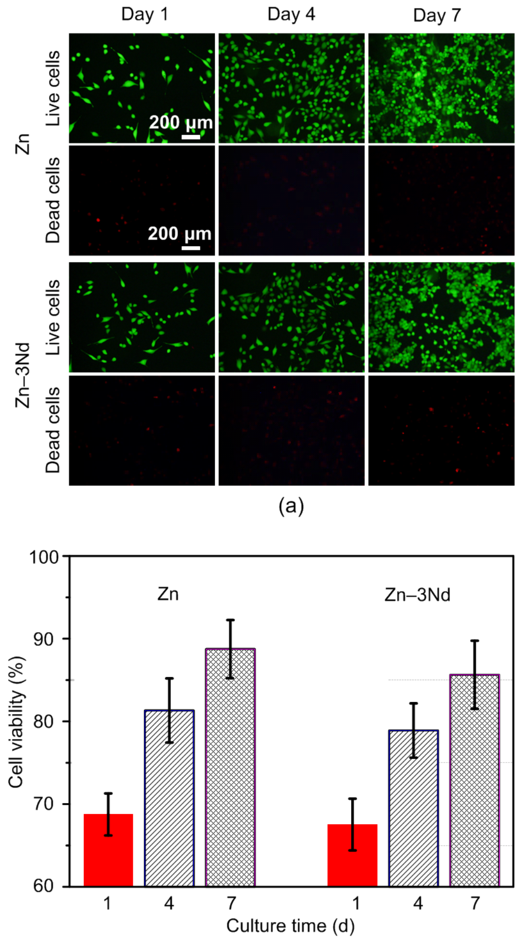

(a)

(b)

Fig. 9 Morphology of MG-63 cells after culture for 1, 4 or 7 d (live cells are stained green and dead cells red) (a) and CCK-8 results for MG-63 cells after culture for 1, 4 or 7 d (b). References to color refer to the online version of this figure

4 Discussion

4.1 Forming quality and microstructural features

It is well known that Zn has a low melting point (420 °C) and boiling point (907 °C). Thus, it is easily vaporized during laser melting, even at optimized process parameters, resulting in severe spatter and porosity (Wang et al., 2017). In this condition, numerous evaporated small-scale particles shelter the partial laser beam, resulting in unstable laser energy deposited on the powder bed. Thus, the molten pool becomes unstable and undergoes insufficient fusion, leading to a discontinuous scanning trace with a rough surface (Fig. 2a). Wen et al. (2018a) developed a circulation system to reduce the interference of Zn vapour on a laser beam, which significantly improved the forming quality (Wen et al., 2018b).

In this study, Nd improved the formation quality of laser additive manufactured Zn part. It appeared that Nd alloying released a large amount of heat, thereby reducing the liquid temperature and creating a narrow crystallization interval (Wang et al., 1999). Nd as a surface active element was able to deoxidize and purify the molten pool (Wang et al., 2018). These two factors contributed to a reduced evaporation of Zn, as well as raised fluidity. According to Marangoni flow theories (Gu et al., 2011),

$$\mathrm{Ma}=\frac{\Delta\gamma\cdot L}{\eta\cdot\tau}, \tag{2}$$

where Ma is the strength of convection movement in molten pool during metal powder melting, $\Delta\gamma$ is the surface tension, L is the freeform surface, and η and τ are the dynamic and kinematic viscosities of the molten pool, respectively. Thus, the raised fluidity with reduced dynamic viscosity favored the production of a smooth surface with a high densification rate for Zn–3Nd. However, excessive Nd released excessive heat, which intensified the Marangoni flow and turbulence within the molten pool. The experiments also confirmed that abundant evaporation of Zn occurred during laser melting of Zn–5Nd. In this condition, the molten pool suffered severe turbulence, resulting in twisted scanning tracks and a reduced densification rate.

The alloying treatment also refined the grain size (Fig. 3). It is thought that Nd with its high surface activity and large atomic volume could form a surfactant film to reduce the surface tension of the liquid phase, thereby reducing the nucleation energy and critical nucleus radius for heterogeneous nucleation (Krivilyov et al., 2012). On the other hand, Nd may gather at the solid/liquid interface during the solidification, forming compositional fluctuation, which contributes to an enhanced compositional supercooling and consequently disrupts primary grain growth (Wu et al., 2013). The Nd-induced precipitated phase is also beneficial for obtaining refined grain (Shuai et al., 2017). In brief, the alloying treatment with Nd improved the forming quality and simultaneously refined the microstructure, which is of great significance for the laser additive manufactured Zn part.

4.2 Influence of alloying treatment on mechanical properties

Sufficient mechanical strength is a prerequisite for bone implants, to provide stable structural support at the early stage of implantation (Shuai et al., 2020f, 2020g; Wang et al., 2020). Herein, the laser additive manufactured Zn–Nd parts had considerably more tensile strength than pure Zn. The improved mechanical strength could be partly attributed to the Nd-induced high densification rate. The densification rate is usually recognized as the primary indicator for evaluating the performance of laser additive manufactured parts. Grain refinement caused by the alloying treatment should also be considered. The Zn–3Nd part had finer grains than the Zn part (Fig. 3c). Such a grain refinement caused by alloying treatment was also reported by other researchers (Gao et al., 2019; Qian et al., 2019). Moreover, Nd partly dissolved in the Zn matrix or precipitated as eutectics, which also contributed to a combination of solid solution strengthening and precipitation strengthening. As observation of the fracture surface revealed, the Zn part presented a typical cleavage fracture mode, whereas the Zn–3Nd part with refined grains and precipitated phases presented a mixed transgranular and intergranular fracture mode. Generally, the enhanced tensile strength of as-built Zn–Nd part can provide stable structural support during implantation. However, the elastic modulus was higher than natural hard bone tissue, which would cause a stress shielding effect. From this point of view, a porous Zn scaffold would be more suitable for bone tissue engineering than solid bone implants. Note that further raising the Nd resulted in decreased mechanical strength. It appeared that the excessively hard brittle precipitates greatly impaired the strength and ductility of the as-built parts. Herein, the obtained elongation of Zn–5Nd was considerably reduced. Similarly, a reduced elongation of Zn–WE43 from 10.1% to 0.9% was also reported (Liang et al., 2019).

4.3 Corrosion behavior and anti-inflammatory activity of Zn–Nd alloy

Apart from Zn, the other two typical degradable metals (Fe and Mg) have also been proposed for bone tissue repair (Shuai et al., 2019a, 2020b). These three types of biodegradable metals undergo the same electrochemical corrosion mechanism in physiological environments, as follows (Li HF et al., 2014):

$$\mathrm{M}+2\mathrm{H}_2\mathrm{O}\rightarrow \mathrm{M}^{2+}+\mathrm{H}_2+2\mathrm{OH}^-, \qquad (3)$$

where M represents Fe, Mg or Zn. The electrode potential of Zn is about −0.76 V, which is between those of Fe (−0.44 V) and Mg (−2.36 V) (Shuai et al., 2020d). This suggests that Zn should degrade in a more mild way than Mg, but faster than Fe in physiological environments. Our results indicated that the Nd alloying treatment reduced the corrosion rate to some extent, and that this effect could be ascribed to Nd-induced grain refinement and an enhanced densification rate. Nevertheless, the degradation rate of Zn was too slow in bulk state. Thus, a Zn bone implant with a porous structure was generally required for bone tissue engineering applications, aiming to match the natural bone growth rate.

Favorable anti-inflammatory activity is also demanded for bone implants, as inflammation readily occurs during bone repair (Yang WJ et al., 2020). In this study, the results clearly showed that the Zn–Nd alloy had good anti-inflammatory activity. Nd^{3+} has a similar ion radius, but more positive charge, than Ca^{2+}, which enable it to replace Ca^{2+} more competitively, to bind with oxygen-containing ligands (carboxyl and hydroxyl groups) (Yin et al., 2011). However, unlike Ca^{2+}, the absorbed Nd^{3+} could not exchange accessories with enzyme molecules, thus obstructing the intracellular Ca signaling and channel opening (Jiang et al., 2013). As a result, pro-inflammatory enzyme activity was reduced, which inhibited the release of pro-inflammatory cytokines, such as IL-1β, IL-6, and TNF-α. On the other hand, Nd^{3+} has a strong affinity with cell membrane phospholipids, and can stabilize on the cell surface and lysosomal membranes (Das et al., 1988; He et al., 2019; Shuai et al., 2020c). In this case, the related signaling pathway such as signal transducer and activator of transcription-3 (STAT3) was activated, and consequently induced the formation of anti-inflammatory cytokine. At the same time, lysosome secretion was also inhibited, which could prevent the destruction of tissue cells and the release of bioactive substances causing inflammation. Thus, Zn–Nd alloy exhibited favorable anti-inflammatory activity, enhancing its potential as a candidate for bone implants.

5 Conclusions

In this study, Zn–Nd parts were fabricated using laser additive manufacturing technology. The effects of Nd on formation quality, mechanical properties, and anti-inflammatory activity were studied. Our conclusions can be summarized as follows:

1. The Nd alloying treatment improved the formation quality of the laser additive manufactured Zn–*x*Nd parts, which achieved a smooth and continuous scanning trace and a high densification rate of 98.71%.

2. Nd addition contributed to grain refinement and second-phase strengthening. The ultimate tensile strength of the Zn–3Nd part was enhanced to (119.3±5.1) MPa. The corrosion resistance of the Zn–Nd parts was also enhanced to a small extent.

3. Nd alloying inhibited the release of pro-inflammatory factors and promoted the release of anti-inflammatory factors, endowing the Zn–Nd parts with good anti-inflammatory activity. Cell culture tests also indicated that they showed no obvious cytotoxicity, with cell viability of 85.6% after 7-d culture.

Contributors

Ci-jun SHUAI, Ming-li YANG, and You-wen YANG designed the study. Ming-li YANG and Shu-ping PENG completed the experiments. Ming-li YANG processed the corresponding data and wrote the first draft of the manuscript. Fang DENG, Fang-wei QI, Chong-xian HE, Li-da SHEN, and Hui-xin LIANG helped to organize the manuscript. Ci-jun SHUAI, Ming-li YANG, and You-wen YANG revised and edited the final version.

Conflict of interest

Ci-jun SHUAI, Ming-li YANG, Fang DENG, You-wen YANG, Shu-ping PENG, Fang-wei QI, Chong-xian HE, Li-da SHEN, and Hui-xin LIANG declare that they have no conflict of interest.

References

ASTM (American Society for Testing and Materials), 2004. Standard Practice for Laboratory Immersion Corrosion Testing of Metals, ASTM G31-72:2004. ASTM, West Conshohocken, USA. https://doi.org/10.1520/G0031-72R04

Baltaci AK, Yuce K, Mogulkoc R, 2018. Zinc metabolism and metallothioneins. *Biological Trace Element Research*, 183(1):22-31.
https://doi.org/10.1007/s12011-017-1119-7

Brooks AJ, Yao H, Yuan J, et al., 2018. Early detection of fracture failure in SLM AM tension testing with Talbot-Lau neutron interferometry. *Additive Manufacturing*, 22: 658-664.
https://doi.org/10.1016/j.addma.2018.06.012

Cao Y, Shi TS, Jiao C, et al., 2020. Fabrication and properties of zirconia/hydroxyapatite composite scaffold based on digital light processing. *Ceramics International*, 46(2): 2300-2308.
https://doi.org/10.1016/j.ceramint.2019.09.219

Das T, Sharma A, Talukder G, 1988. Effects of lanthanum in cellular systems. *Biological Trace Element Research*, 18(1):201-228.
https://doi.org/10.1007/BF02917504

Gao CD, Yao M, Shuai CJ, et al., 2019. Nano-Sic reinforced Zn biocomposites prepared via laser melting: microstructure, mechanical properties and biodegradability. *Journal of Materials Science & Technology*, 35(11): 2608-2617.
https://doi.org/10.1016/j.jmst.2019.06.010

Gu DD, Hagedorn YC, Meiners W, et al., 2011. Nanocrystalline TiC reinforced Ti matrix bulk-form nanocomposites by selective laser melting (SLM): densification, growth mechanism and wear behavior. *Composites Science and Technology*, 71(13):1612-1620.
https://doi.org/10.1016/j.compscitech.2011.07.010

He SW, Yang S, Zhang YR, et al., 2019. LncRNA ODIR1 inhibits osteogenic differentiation of hUC-MSCs through the FBXO25/H2BK120ub/H3K4me3/OSX axis. *Cell Death & Disease*, 10(12):947.
https://doi.org/10.1038/s41419-019-2148-2

Hou Y, Jia GZ, Yue R, et al., 2018. Synthesis of biodegradable Zn-based scaffolds using NaCl templates: relationship between porosity, compressive properties and degradation behavior. *Materials Characterization*, 137:162-169.
https://doi.org/10.1016/j.matchar.2018.01.033

ISO (International Organization for Standardization), 2009. Biological Evaluation of Medical Devices—Part 5: Tests for in Vitro Cytotoxicity, ISO 10993-5:2009. ISO, Geneva, Switzerland.

ISO (International Organization for Standardization), 2019. Plastics—Determination of Tensile Properties—Part 1: General Principles, ISO 527-1:2019. ISO, Geneva, Switzerland.

Jiang C, Zou Y, Liu X, et al., 2013. Dose-dependent effects of lanthanum chloride on wear particle-induced aseptic inflammation in a murine air-pouch model. *Journal of Rare Earths*, 31(4):420-427.
https://doi.org/10.1016/S1002-0721(12)60298-1

Jin L, Chen CX, Li YT, et al., 2019. A biodegradable Mg-based alloy inhibited the inflammatory response of THP-1 cell-derived macrophages through the TRPM7-PI3K-AKT1 signaling axis. *Frontiers in Immunology*, 10: 2798.
https://doi.org/10.3389/fimmu.2019.02798

Krivilyov M, Volkmann T, Gao J, et al., 2012. Multiscale analysis of the effect of competitive nucleation on phase selection in rapid solidification of rare-earth ternary magnetic materials. *Acta Materialia*, 60(1):112-122.
https://doi.org/10.1016/j.actamat.2011.09.009

Li HF, Zheng YF, Qin L, 2014. Progress of biodegradable metals. *Progress in Natural Science: Materials International*, 24(5):414-422.
https://doi.org/10.1016/j.pnsc.2014.08.014

Li P, Schille C, Schweizer E, et al., 2019. Selection of extraction medium influences cytotoxicity of zinc and its alloys. *Acta Biomaterialia*, 98:235-245.
https://doi.org/10.1016/j.actbio.2019.03.013

Li RB, Ji ZX, Qin HQ, et al., 2014. Interference in autophagosome fusion by rare earth nanoparticles disrupts autophagic flux and regulation of an interleukin-1β producing inflammasome. *ACS Nano*, 8(10):10280-10292.
https://doi.org/10.1021/nn505002w

Li W, Jiang HX, Zhang LL, et al., 2019. Solidification of Al-Bi-Sn immiscible alloy under microgravity conditions of space. *Scripta Materialia*, 162:426-431.
https://doi.org/10.1016/j.scriptamat.2018.12.010

Liang HX, Yang YW, Xie DQ, et al., 2019. Trabecular-like Ti-6Al-4V scaffolds for orthopedic: fabrication by selective laser melting and in vitro biocompatibility. *Journal of Materials Science & Technology*, 35(7):1284-1297.
https://doi.org/10.1016/j.jmst.2019.01.012

Liu J, Gu DD, Chen HY, et al., 2018. Influence of substrate surface morphology on wetting behavior of tracks during selective laser melting of aluminum-based alloys. *Journal of Zhejiang University-SCIENCE A (Applied Physics & Engineering)*, 19(2):111-121.
https://doi.org/10.1631/jzus.A1700599

Montani M, Demir AG, Mostaed E, et al., 2017. Processability of pure Zn and pure Fe by SLM for biodegradable metallic implant manufacturing. *Rapid Prototyping Journal*, 23(3):514-523.
https://doi.org/10.1108/RPJ-08-2015-0100

Niu JL, Tang ZB, Huang H, et al., 2016. Research on a Zn-Cu alloy as a biodegradable material for potential vascular stents application. *Materials Science and Engineering: C*, 69:407-413.
https://doi.org/10.1016/j.msec.2016.06.082

Pariona MM, Micene KT, 2019. Effect of microstructure on microhardness and electrochemical behavior in hypereutectic Al-Fe alloy processed by laser surface remelting. *In*: Dekoulis G (Ed.), Aerospace Engineering. IntechOpen, London, UK.
https://doi.org/10.5772/intechopen.81095

Paz R, Monzón MD, Bertrand P, et al., 2019. Comparison of different cellular structures for the design of selective laser melting parts through the application of a new lightweight parametric optimisation method. *Journal of*

Zhejiang University-SCIENCE A (Applied Physics & Engineering), 20(2):117-132.
https://doi.org/10.1631/jzus.A1800422

Plotkowski A, Rios O, Sridharan N, et al., 2017. Evaluation of an Al-Ce alloy for laser additive manufacturing. *Acta Materialia*, 126:507-519.
https://doi.org/10.1016/j.actamat.2016.12.065

Qian XY, Zeng Y, Jiang B, et al., 2019. Grain refinement mechanism and improved mechanical properties in Mg–Sn alloy with trace Y addition. *Journal of Alloys and Compounds*, 820:153122.
https://doi.org/10.1016/j.jallcom.2019.153122

Shi MC, Xia LG, Chen ZT, et al., 2017. Europium-doped mesoporous silica nanosphere as an immune-modulating osteogenesis/angiogenesis agent. *Biomaterials*, 144:176-187.
https://doi.org/10.1016/j.biomaterials.2017.08.027

Shuai CJ, Yang YW, Peng SP, et al., 2017. Nd-induced honeycomb structure of intermetallic phase enhances the corrosion resistance of Mg alloys for bone implants. *Journal of Materials Science: Materials in Medicine*, 28(9):130.
https://doi.org/10.1007/s10856-017-5945-0

Shuai CJ, Li YL, Yang YW, et al., 2019a. Bioceramic enhances the degradation and bioactivity of iron bone implant. *Materials Research Express*, 6(11):115401.
https://doi.org/10.1088/2053-1591/ab45b9

Shuai CJ, Liu GF, Yang YW, et al., 2019b. Construction of an electric microenvironment in piezoelectric scaffolds fabricated by selective laser sintering. *Ceramics International*, 45(16):20234-20242.
https://doi.org/10.1016/j.ceramint.2019.06.296

Shuai CJ, Yu L, Feng P, et al., 2020a. Interfacial reinforcement in bioceramic/biopolymer composite bone scaffold: the role of coupling agent. *Colloids and Surfaces B: Biointerfaces*, 193:111083.
https://doi.org/10.1016/j.colsurfb.2020.111083

Shuai CJ, Wang B, Bin SZ, et al., 2020b. Interfacial strengthening by reduced graphene oxide coated with MgO in biodegradable Mg composites. *Materials & Design*, 191: 108612.
https://doi.org/10.1016/j.matdes.2020.108612

Shuai CJ, Cheng Y, Yang WJ, et al., 2020c. Magnetically actuated bone scaffold: microstructure, cell response and osteogenesis. *Composites Part B: Engineering*, 192: 107986.
https://doi.org/10.1016/j.compositesb.2020.107986

Shuai CJ, Li S, Yang WJ, et al., 2020d. MnO_2 catalysis of oxygen reduction to accelerate the degradation of Fe-C composites for biomedical applications. *Corrosion Science*, 170:108679.
https://doi.org/10.1016/j.corsci.2020.108679

Shuai CJ, Dong Z, He CX, et al., 2020e. A peritectic phase refines the microstructure and enhances Zn implants. *Journal of Materials Research and Technology*, 9(3): 2623-2634.
https://doi.org/10.1016/j.jmrt.2020.04.037

Shuai CJ, Liu GG, Yang YW, et al., 2020f. A strawberry-like Ag-decorated barium titanate enhances piezoelectric and antibacterial activities of polymer scaffold. *Nano Energy*, 74:104825.
https://doi.org/10.1016/j.nanoen.2020.104825

Shuai CJ, Wang B, Bin SZ, et al., 2020g. TiO_2-induced in situ reaction in graphene oxide-reinforced AZ61 biocomposites to enhance the interfacial bonding. *ACS Applied Materials & Interfaces*, 12(20):23464-23473.
https://doi.org/10.1021/acsami.0c04020

Tang ZB, Huang H, Niu JL, et al., 2017. Design and characterizations of novel biodegradable Zn-Cu-Mg alloys for potential biodegradable implants. *Materials & Design*, 117:84-94.
https://doi.org/10.1016/j.matdes.2016.12.075

Wang D, Wu SB, Fu F, et al., 2017. Mechanisms and characteristics of spatter generation in SLM processing and its effect on the properties. *Materials & Design*, 117:121-130.
https://doi.org/10.1016/j.matdes.2016.12.060

Wang GY, He CX, Yang WJ, et al., 2020. Surface-modified graphene oxide with compatible interface enhances poly-L-lactic acid bone scaffold. *Journal of Nanomaterials*, 2020:5634096.
https://doi.org/10.1155/2020/5634096

Wang MF, Xiao DH, Zhou PF, et al., 2018. Effects of rare earth yttrium on microstructure and properties of Mg-Al-Zn alloy. *Journal of Alloys and Compounds*, 742: 232-239.
https://doi.org/10.1016/j.jallcom.2018.01.234

Wang P, Liu J, Shen S, et al., 2019. In vitro and in vivo studies on two-step alkali-fluoride-treated Mg-Zn-Y-Nd alloy for vascular stent application: enhancement in corrosion resistance and biocompatibility. *ACS Biomaterials Science & Engineering*, 5(7):3279-3292.
https://doi.org/10.1021/acsbiomaterials.9b00140

Wang QD, Lu YZ, Zeng XQ, et al., 1999. Study on the fluidity of AZ91+xRE magnesium alloy. *Materials Science and Engineering: A*, 271(1-2):109-115.
https://doi.org/10.1016/S0921-5093(99)00185-9

Wei KW, Zeng XY, Wang ZM, et al., 2019. Selective laser melting of Mg-Zn binary alloys: effects of Zn content on densification behavior, microstructure, and mechanical property. *Materials Science and Engineering: A*, 756: 226-236.
https://doi.org/10.1016/j.msea.2019.04.067

Wen P, Jauer L, Voshage M, et al., 2018a. Densification behavior of pure Zn metal parts produced by selective laser melting for manufacturing biodegradable implants. *Journal of Materials Processing Technology*, 258:128-137.
https://doi.org/10.1016/j.jmatprotec.2018.03.007

Wen P, Voshage M, Jauer L, et al., 2018b. Laser additive manufacturing of Zn metal parts for biodegradable applications: processing, formation quality and mechanical properties. *Materials & Design*, 155:36-45. https://doi.org/10.1016/j.matdes.2018.05.057

Wu XF, Zhang GA, Wu FF, et al., 2013. Influence of neodymium addition on microstructure, tensile properties and fracture behavior of cast Al-Mg$_2$Si metal matrix composite. *Journal of Rare Earths*, 31(3):307-312. https://doi.org/10.1016/S1002-0721(12)60277-4

Xu XY, Chen XH, Du WW, et al., 2017. Effect of Nd on microstructure and mechanical properties of as-extruded Mg-Y-Zr-Nd alloy. *Journal of Materials Science & Technology*, 33(9):926-934. https://doi.org/10.1016/j.jmst.2017.04.011

Yang WJ, Zhong YC, He CX, et al., 2020. Electrostatic self-assembly of *p*FE$_3$O$_4$ nanoparticles on graphene oxide: a co-dispersed nanosystem reinforces PLLA scaffolds. *Journal of Advanced Research*, 24:191-203. https://doi.org/10.1016/j.jare.2020.04.009

Yang YW, Yuan FL, Gao CD, et al., 2018. A combined strategy to enhance the properties of Zn by laser rapid solidification and laser alloying. *Journal of the Mechanical Behavior of Biomedical Materials*, 82:51-60. https://doi.org/10.1016/j.jmbbm.2018.03.018

Yang YW, He CX, E DY, et al., 2020. Mg bone implant: features, developments and perspectives. *Materials & Design*, 185:108259. https://doi.org/10.1016/j.matdes.2019.108259

Yang YW, Cheng Y, Peng SP, et al., 2021. Microstructure evolution and texture tailoring of reduced graphene oxide reinforced Zn scaffold. *Bioactive Materials*, 6(5):1230-1241. https://doi.org/10.1016/j.bioactmat.2020.10.017

Yao CZ, Wang ZC, Tay SL, et al., 2014. Effects of Mg on microstructure and corrosion properties of Zn–Mg alloy. *Journal of Alloys and Compounds*, 602:101-107. https://doi.org/10.1016/j.jallcom.2014.03.025

Yao H, Zhang YJ, Liu L, et al., 2016. Inhibition of lanthanide nanocrystal-induced inflammasome activation in macrophages by a surface coating peptide through abrogation of ROS production and TRPM2-mediated Ca^{2+} influx. *Biomaterials*, 108:143-156. https://doi.org/10.1016/j.biomaterials.2016.08.036

Yin HY, Xu LB, Porter NA, 2011. Free radical lipid peroxidation: mechanisms and analysis. *Chemical Reviews*, 111(10):5944-5972. https://doi.org/10.1021/cr200084z

Yue R, Zhang J, Ke GZ, et al., 2019. Effects of extrusion temperature on microstructure, mechanical properties and in vitro degradation behavior of biodegradable Zn-3Cu-0.5Fe alloy. *Materials Science and Engineering: C*, 105: 110106. https://doi.org/10.1016/j.msec.2019.110106

Zhu DY, Lu B, Yin JH, et al., 2019. Gadolinium-doped bioglass scaffolds promote osteogenic differentiation of hBMSC via the Akt/GSK3β pathway and facilitate bone repair in vivo. *International Journal of Nanomedicine*, 14:1085-1100. https://doi.org/10.2147/IJN.S193576

Zhu SM, Wu CC, Li GN, et al., 2019. Creep properties of biodegradable Zn-0.1Li alloy at human body temperature: implications for its durability as stents. *Materials Research Letters*, 7(9):347-353. https://doi.org/10.1080/21663831.2019.1610106

Zhu Y, Zou J, Yang HY, 2018. Wear performance of metal parts fabricated by selective laser melting: a literature review. *Journal of Zhejiang University-SCIENCE A (Applied Physics & Engineering)*, 19(2):95-110. https://doi.org/10.1631/jzus.A1700328

中文概要

题　目： **增材制造制备 Zn–Nd 合金的成形质量、力学性能及抗炎活性**

目　的： 锌具有良好的降解性能和生物相容性，被视为一种很有前途的骨修复材料。然而，锌金属作为骨植入物时的力学强度难以满足承重骨修复的需求，并存在炎症反应的风险。本文旨在探讨稀土钕合金化对锌骨植入物激光成形质量的影响，为改善锌合金的成形质量、提高力学性能及增加抗炎活性提供理论依据。

创新点： 1. 在增材制造过程中，添加钕能够有效改善锌基合金的成形质量；2. 稀土钕提高了锌基合金的力学性能，同时也赋予了抗炎活性。

方　法： 1. 通过实验对比锌钕合金的表面形貌，计算出相应的致密度，并分析钕对锌基合金成形质量的影响（图 2）；2. 基于不同实验对比锌钕合金的微观组织结构及力学强度的变化，并探讨稀土钕提高力学性能的原因（图 3~5 和表 1）；3. 通过电化学实验和浸泡实验，分析稀土钕对降解性能的影响（图 6 和 7）；4. 基于体外生物学实验，对比分析钕对抗炎活性和细胞活性的影响（图 8 和 9）。

结　论： 1. 稀土钕提高了激光增材制造锌合金的成形质量，并使其致密化率高达 98.71%；2. 钕合金化有助于晶粒细化和第二相强化，使极限抗拉强度提高到了(119.3±5.1) MPa；3. 钕合金化能抑制促炎因子的释放，促进抗炎因子的释放，进而使锌钕部分具有良好的抗炎活性，而细胞培养试验也表明其具有良好的生物相容性。

关键词： 锌钕合金；激光粉末熔融；抗炎活性；力学性能